High-Efficiency Input and Output Harmonically Engineered Power Amplifiers

Tushar Sharma, *Member, IEEE*, Srinidhi E. R., Ramzi Darraji, *Member, IEEE*, Damon G. Holmes, *Member, IEEE*, Joseph Staudinger, *Fellow, IEEE*, Jeffrey K. Jones, *Senior Member, IEEE*, and Fadhel M. Ghannouchi, *Fellow, IEEE*

***Abstract*— This paper presents an in-depth, systematic study of the impact of input and output harmonics in the design of high-efficiency power amplifiers (PAs). The study evaluates the performance of harmonically tuned amplifiers, tackling concurrently both input and output harmonics. The proposed theory starts with deriving an altered input voltage waveform under the impact of input nonlinearity. Intrinsic drain voltage and drain current components are formulated as a function of the conduction angle α considering both source and load terminations. Output power and drain efficiency are then computed as a function of input nonlinearity, α, and output loading conditions. The derived formulations allow to investigate the design sensitivity to input nonlinearity and its impact on fundamental design space. The impact of source harmonics is evaluated using harmonic source pull under different output loading conditions. Thereafter, PA design and implementation has been carried out using NXP 1.95 mm die to confirm the distinctive behavior of class GF and GF^{-1} amplifiers with respect to the input harmonic terminations. For practical validation, four different design cases with different second harmonic source impedances are investigated. At 2.6 GHz, drain efficiencies ranging between 76% and 83% were exhibited depending on the source and load harmonic tuning for each design case. Measurement results confirm the theoretical findings reported in this paper.**

***Index Terms*— Class F, class F^{-1}, class GF, class GF^{-1}, gallium nitride (GaN), harmonic tuned (HT), high efficiency, input waveform shaping, load–pull, power amplifiers (PAs).**

I. Introduction

THE high-efficiency power amplifier (PA) design is increasingly becoming an integral part of wireless communication systems. The cellular base station market is slowly transitioning to gallium-nitride (GaN)-based RF products to meet the expected fifth generation (5G) communication. The next generation of wireless systems, now called 5G, have been projected to deliver, amongst other benefits, improved reliability, lower latency, increased user experienced data rate, higher area traffic capacity, and increased network energy efficiency [1]. Critical to the enablement of the next generation RF electronics continues to be the PA—the last gain block of the transmit chain. Improvement of its performance characteristics of gain, output power, linearity, and dc-RF conversion efficiency remain a focus for researchers now within the context of stringent massive multiple input multiple output 5G requirements.

With the achievement of large advances in the cellular infrastructure industry, high cutoff frequency devices such as gallium arsenide (GaAs), GaN high-electron-mobility transistors (HEMTs) have accelerated the output harmonic manipulation methods, to achieve better control over harmonic frequencies thus yielding higher efficiency [2]–[9]. Class F which has infinite third harmonic manipulation and inverse Class F (F^{-1}) which has infinite second harmonic manipulation are popular representatives of harmonically tuned (HT) PAs. To date, some previous works on HT amplifiers like Class F and Class F^{-1} PA design and implementation have shown very good performance in terms of drain efficiency (DE) [3]–[8]. In these works, the emphasis was on the optimization of the output harmonic terminations to shape the waveforms at the drain of the device.

That said, in the vast majority of previously reported works [2]–[6], there is no clear understanding of the impact of input harmonic tuning on the behavior of those HT amplifiers because, in most cases, an ideal sinusoidal excitation is assumed at the input. Several attempts have demonstrated HT-PA design with harmonic source– and load–pull techniques [10]–[17]. However, a comprehensive time domain waveform-based theory illustrating the behavior of Class F and Class F^{-1} amplifiers under input harmonic conditions is lacking.

This paper targets extending the design of HT amplifiers to consider both input and output harmonic terminations based on large-signal time domain waveforms. Specifically, the correlation between input and output harmonic conditions is studied thoroughly for Class F and Class F^{-1} amplifiers for all conduction angles. A simplified block diagram of an input and output harmonically engineered PA is shown in Fig. 1. This investigation reveals that Class F and Class F^{-1} amplifiers

Manuscript received April 27, 2017; revised August 4, 2017; accepted September 12, 2017. Date of publication October 13, 2017; date of current version February 5, 2018. This work was supported in part by the Natural Sciences and Engineering Research Council of Canada, in part by Alberta Innovates Technology Futures, and in part by the Canada Research Chairs Program. *(Corresponding author: Tushar Sharma.)*

T. Sharma is with the Intelligent RF Radio Laboratory, Department of Electrical and Computer Engineering, University of Calgary, Calgary, AB T2N 1N4, Canada, and also with the NXP Semiconductors, Chandler, AZ 85224 USA (e-mail: tsharm@ucalgary.ca).

Srinidhi E. R., D. G. Holmes, J. Staudinger, and J. K. Jones are with the NXP Semiconductors, Chandler, AZ 85224 USA (e-mail: ramanujam.embar@nxp.com; damon.holmes@nxp.com; joseph.staudinger@nxp.com; j.jones@nxp.com).

R. Darraji and F. M. Ghannouchi are with the Intelligent RF Radio Laboratory, Department of Electrical and Computer Engineering, University of Calgary, Calgary, AB T2N 1N4, Canada (e-mail: rdarraji@ucalgary.ca; fadhel.ghannouchi@ucalgary.ca).

Color versions of one or more of the figures in this paper are available online at http://ieeexplore.ieee.org.

Digital Object Identifier 10.1109/TMTT.2017.2756046

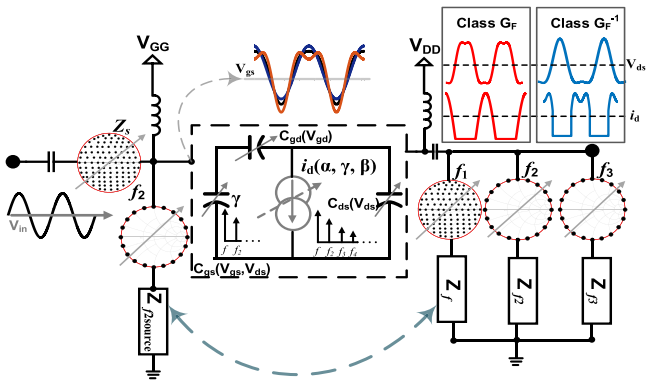

Fig. 1. Simplified diagram of an input and output harmonically engineered PA.

have significantly dissimilar behavior with respect to the input harmonic terminations. For instance, while it is very critical in a Class F amplifier to tune the input harmonic to achieve the anticipated RF performance, the Class F^{-1} amplifier, on the other hand, is demonstrated to be capable of maintaining close to maximal performance regardless of the second harmonic condition at the input. The causes of such dissimilar behavior are to be explained in later sections. Besides, since input harmonic conditions are impacted by the gate–source capacitance (C_{gs}) of the device, the comprehensive study presented in this paper also considers impact of C_{gs} on the overall performance of HT amplifiers.

This paper is organized as follows. In Section II, a generalized theory that simultaneously tackles both input and output harmonic tuning in Class F and Class F^{-1} HT amplifiers is presented. The theoretical performance of those amplifiers is then analyzed thoroughly in Section III. A proof of concept and PA implementation is carried out in Section IV.

II. Input Waveform Shaping

High-efficiency PA operation is achieved by terminating harmonics at the load, which shapes the drain waveforms. The HT PAs (e.g., class F, class F^{-1}) also assume an idealized scenario where the amplifier is driven with a sinusoidal wave. However, this idealized scenario is altered not only by nonlinear current generator but also the gate–source capacitance (C_{gs}) which generates second order harmonic current component. In fact, C_{gs} varies as a function of both gate–source voltage (V_{gs}) and the drain–source-voltage (V_{ds}). However, for a typical GaN device, the measured percentage change in C_{gs} with respect to varying V_{ds} is significantly lower compared to V_{gs} as inferred from Fig. 2(a) and (b). As a result, the input nonlinearity contribution from C_{gs} is mainly dominated by its dependence on V_{gs}. The Volterra series analysis of input circuit shows that the nonlinearity arising from C_{gs} is mainly responsible for the generation of harmonic components at the input of the device. In large-signal operation, C_{gs} exhibits a major out-of-phase second harmonic content that alters the input sinusoidal waveform [18]–[20].

The generalized gate voltage with second harmonic voltage component at the gate node can be written as a function

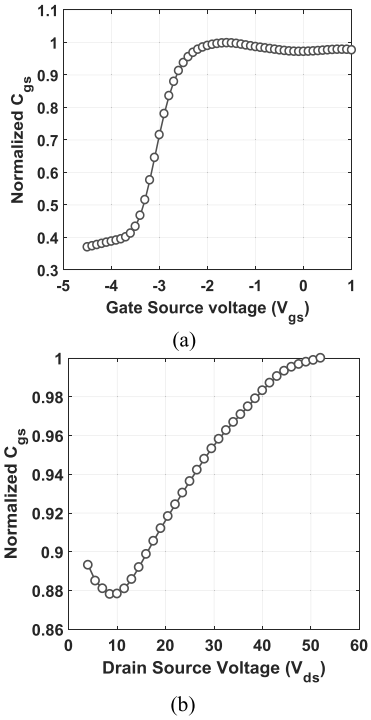

Fig. 2. Measured gate–source capacitance for a typical GaN device. (a) Normalized C_{gs} as a function of gate voltage for a fixed V_{ds}. (b) Normalized C_{gs} as a function of V_{ds} for a fixed pinch-off gate voltage.

of gate bias voltage (V_{gso}), fundamental voltage component (V_1), second harmonic voltage component (V_2), conduction angle (α), and angular frequency (θ) as

$$V_{gs}(\theta,\alpha) = V_{gso} + V_1\left(\frac{\cos\theta - \cos\frac{\alpha}{2}}{1-\cos\frac{\alpha}{2}}\right) + V_2\cos 2\theta. \quad (1)$$

Rearranging the terms and normalizing the input gate voltage by V_1, the normalized gate voltage $\overline{V_{gs}(\theta,\ \alpha,\ \gamma)}$ can be expressed as

$$\overline{V_{gs}(\theta,\alpha,\gamma)} = \frac{V_{gs}(\theta,\alpha) - V_{gso}}{V_1} = \left(\frac{\cos\theta - \cos\left(\frac{\alpha}{2}\right)}{1-\cos\left(\frac{\alpha}{2}\right)}\right) + \gamma\cos 2\theta \quad (2)$$

where $\gamma = V_2/V_1$ is the voltage ratio of the second harmonic and fundamental voltage component. Also, it is noteworthy that V_2 and V_1 exhibit an out-of-phase relationship, thus $\gamma < 0$. For the ideal case ($\gamma = 0$), the input voltage varies as a function of α as shown in Fig. 3. However, in operation of high-efficiency PA, an increase in γ generates a major out-of-phase second harmonic component that alters the ideal sinusoidal input waveform ($\gamma = 0$) as depicted in Fig. 4.

Depending on the transconductance (g_m) of the device, the gate input voltage is translated as drain current at the output. Since the waveform shape changes from the ideal sinusoidal excursion, the drain current components are altered thereby impacting the performance of HT amplifiers.

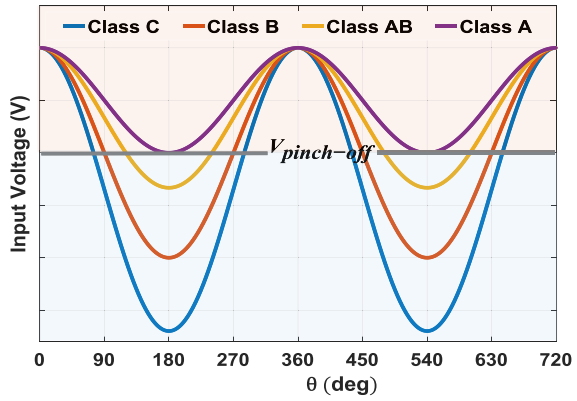

Fig. 3. Normalized input voltage (V_{gs}) with respect to different bias conditions, class C ($\alpha < 180°$), class B ($\alpha = 180°$), class AB ($180 < \alpha < 360°$), and class A ($\alpha = 360°$) for $\gamma = 0$ i.e., no input harmonic nonlinearity.

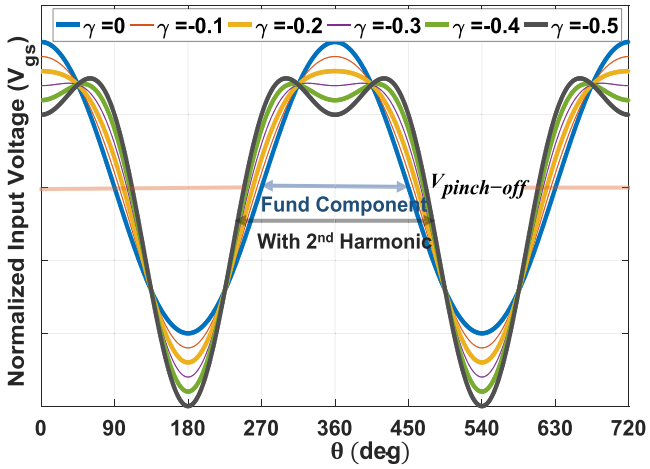

Fig. 4. Input gate voltage waveform of PA with varying second harmonic factor (γ) for $\alpha = 180°$.

A. Gate Bias Cutoff Angle With Input Nonlinearity

The identification of quiescent bias point is performed in terms of device output conduction angle i.e., the fraction of RF signal period where a nonzero current is flowing. The bias selection i.e., class A, class AB, class B, or class C, in turn, defines where the device starts to conduct at, below and above pinch-off gate voltage. In the case of an ideal sinusoidal input excitation, this cutoff angle is generally considered as $\alpha/2$. Conversely, under the impact of nonlinear C_{gs}, the period of nonzero current varies significantly as a function of γ. By forcing (1) to zero, this cutoff angle, β can be derived as a function of α, γ

$$\beta\ (\alpha, \gamma) = \cos^{-1}\left(\frac{\frac{-1}{1-\cos\frac{\alpha}{2}} + \sqrt{\left(\frac{-1}{1-\cos\frac{\alpha}{2}}\right)^2 + 8\gamma\left(\gamma + \frac{\cos\frac{\alpha}{2}}{1-\cos\frac{\alpha}{2}}\right)}}{4\gamma}\right), \quad \text{if } \gamma < 0$$
$$\frac{\alpha}{2}, \quad \text{if } \gamma = 0. \tag{3}$$

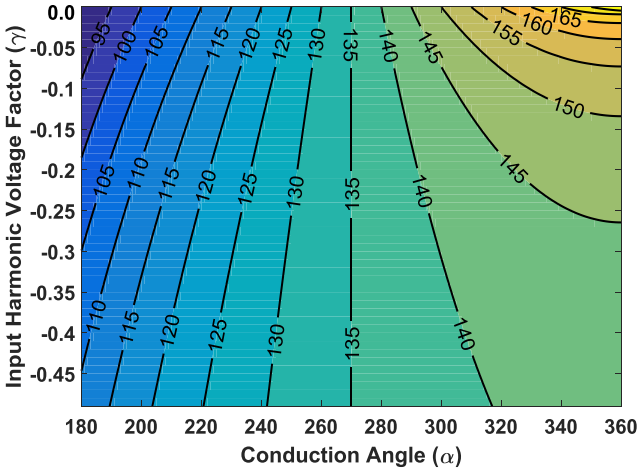

Fig. 5. Zero-crossing cutoff angle (β) with respect to conduction angle (α) and the input harmonic voltage factor (γ).

As can be inferred from Fig. 4, this cutoff angle changes both with α and γ, respectively. Using (3), β can be plotted as a function of γ for different α. Under class B ($\alpha = 180°$), β expands from 90° to 111.5° when γ varies from 0 to −0.5. For class AB bias with ($180° < \alpha < 270°$), β expands as a function of γ; conversely it contracts for ($270° < \alpha < 360°$) as presented in Fig. 5. β is an important parameter to evaluate the drain performance based on the output loading condition and the device operating point.

III. Drain Waveforms and Performance Evaluation

The input voltage at gate node is altered by the harmonic component contribution from C_{gs}. As a result, the waveform is truncated by the cutoff angle derived in Section II. It is noteworthy that the generation of current components due to truncation is not only dependent on the α, but also on the input nonlinearity, or the source harmonic match, and the output loading conditions. As a result, the input and output matching network harmonic response have significant dependence on how this harmonic content is controlled at the current generator of the device. Accordingly, the generalized PA operation class GF and class GF^{-1} are presented under the impact of γ, α and the output loading condition i.e., second harmonic (Z_{2L}), and third harmonic (Z_{3L}).

A. Generalized Class GF Amplifier

Considering the first three harmonics, a generalized class GF can be defined for the Z_{2L} as short Z_{3L} as open circuited. The design of class GF amplifier considers the impact of input nonlinearity for different conduction angles, which allows for modeling the behavior of HT PA considering both source and load terminations. Conventional class F is a special case when the input is driven with a pure sinusoidal wave (i.e., $\gamma = 0$). The HT square output voltage waveform for class GF voltage [21]–[23] is given by $V_{GF}(\theta)$ as

$$V_{GF}(\theta) = \left(1 - \frac{2}{\sqrt{3}}\cos\theta + \frac{1}{3\sqrt{3}}\cos 3\theta\right). \tag{4}$$

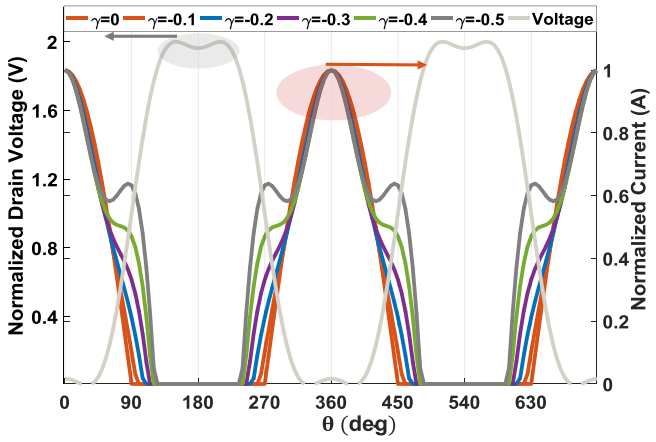

Fig. 6. Class GF drain voltage and current waveforms as a function of γ for class B ($\alpha = 180°$).

The class GF drain current waveform varies with γ, leading to asymmetrical waveforms with different cutoff angles determined using (5) as shown in Fig. 6. Under the class GF PA configuration, by limiting drain current to the peak current (I_m), the drain current ($i_{\rm GF}$) can be formulated as a function of (α), (θ), (γ), and can be written as

$$\begin{aligned} &i_{\rm GF}(\theta,\alpha,\gamma,I_m)\\ &\quad=\left(\frac{I_m+i_{r3}(\alpha,\beta,\gamma,I_m)}{1+\gamma}\right)\\ &\qquad\times\left(\frac{\cos\theta-\cos\left(\frac{\alpha}{2}\right)}{1-\cos\left(\frac{\alpha}{2}\right)}+\gamma\cos 2\theta\right)\\ &\qquad-i_{r3}(\alpha,\beta,\gamma,I_m)\cos 3\theta;\\ &\qquad-\beta(\alpha,\gamma)\le\theta\le\beta(\alpha,\gamma)\\ &\qquad 0;\quad -\pi<\theta<-\beta(\alpha,\gamma),\beta(\alpha,\gamma)<\theta<\pi. \end{aligned} \tag{5}$$

For class GF PAs, the third harmonic current component in $i_{\rm GF}$ should be zero due to an open circuit harmonic impedance. By imposing the boundary condition as in (6), $i_{r3}(\alpha,\beta,\gamma,I_m)$, the real part of third harmonic drain current can be computed as a function of α, γ, I_m and is given by (7), shown at the bottom of the this page,

$$\frac{1}{\pi}\int_{-\beta\ (\alpha,\gamma)}^{\beta\ (\alpha,\gamma)} i_{\rm GF}(\theta,\alpha,\gamma,I_m)\cdot\cos 3\theta d\theta=0. \tag{6}$$

By applying the Fourier expansion of $i_{\rm GF}$ given in (5), the dc ($i_{\rm GF,dc}$), fundamental ($i_{\rm GF,1}$), second ($i_{\rm GF,2}$) and third harmonic ($i_{\rm GF,3}$) current components can be computed as

$$\begin{aligned} &i_{\rm GF,dc}(\alpha,\beta,\gamma,I_m)\\ &=\frac{1}{2\pi}\left(\frac{I_m+i_{r3}(\alpha,\beta,\gamma,I_m)}{1+\gamma}\right)\\ &\quad\times\left(\frac{2\beta\cos\frac{\alpha}{2}-2\sin\beta}{\cos\left(\frac{\alpha}{2}\right)-1}+\gamma\sin 2\beta\right)\\ &\quad-\frac{i_{r3}(\alpha,\beta,\gamma,I_m)\sin 3\beta}{3\pi} \end{aligned} \tag{8}$$

$$\begin{aligned} &i_{\rm GF,1}(\alpha,\beta,\gamma,I_m)\\ &=\frac{1}{\pi}\left(\frac{I_m+i_{r3}(\alpha,\beta,\gamma,I_m)}{1+\gamma}\right)\\ &\quad\times\left(2\gamma\sin\beta-\frac{4}{3}\gamma\sin^3\beta-\frac{\left(\beta+\frac{\sin 2\beta}{2}\right)}{\cos\left(\frac{\alpha}{2}\right)-1}+\frac{2\sin\beta\cos\left(\frac{\alpha}{2}\right)}{\cos\left(\frac{\alpha}{2}\right)-1}\right)\\ &\quad-\frac{2i_{r3}(\alpha,\beta,\gamma,I_m)\sin\beta\cos^3\beta}{\pi} \end{aligned} \tag{9}$$

$$\begin{aligned} &i_{\rm GF,2}(\alpha,\beta,\gamma,I_m)\\ &=\frac{1}{\pi}\left(\frac{I_m+i_{r3}(\alpha,\beta,\gamma,I_m)}{1+\gamma}\right)\\ &\quad\times\left(\gamma\left(\beta+\frac{\sin 4\beta}{4}\right)\frac{-\left(2\sin\beta-\frac{4}{3}\sin^3\beta\right)+\sin 2\beta\cos\left(\frac{\alpha}{2}\right)}{\cos\left(\frac{\alpha}{2}\right)-1}\right)\\ &\quad-\frac{i_{r3}(\alpha,\beta,\gamma,I_m)}{\pi}\left(\sin\beta+\frac{\sin 5\beta}{5}\right) \end{aligned} \tag{10}$$

$$\begin{aligned} &i_{\rm GF,3}(\alpha,\beta,\gamma,I_m)\\ &=\frac{1}{\pi}\left(\frac{I_m+i_{r3}(\alpha,\beta,\gamma,I_m)}{1+\gamma}\right)\\ &\quad\times\left(\frac{\frac{2}{3}\sin 3\beta\cos\left(\frac{\alpha}{2}\right)-2\ sin\beta\cos^3\beta}{\cos\left(\frac{\alpha}{2}\right)-1}+\gamma\left(\sin\beta+\frac{\sin 5\beta}{5}\right)\right)\\ &\quad-\frac{i_{r3}(\alpha,\beta,\gamma,I_m)}{\pi}\left(\beta+\frac{\sin 6\beta}{6}\right). \end{aligned} \tag{11}$$

Using (7)–(11), the drain harmonic components are plotted in Fig. 7 as a function of α and γ. The dc current component increases significantly with increase of γ, along with change in fundamental and second harmonic current component for different α ($180°, 240°, 360°$) as shown in Fig. 7. The third harmonic current component is zero for any variation in γ for class GF PA operation. For $\gamma=0$, $i_{\rm GF,dc}=1/\pi$, $i_{\rm GF,1}=1/2$, $i_{\rm GF,2}=2/3\pi$, and $i_{\rm GF,3}=0$ which are the same as half-sinusoidal current components under class F PA operation [22], [23].

B. Class GF^{-1} Amplifier

The generalized class $\rm GF^{-1}$ PA mode is achieved when an infinite Z_{2L} and short circuited Z_{3L} is presented at the current plane of the device. An open circuit condition at drain and its interaction with input nonlinearity alters the

$$i_{r3}(\alpha,\beta,\gamma,I_m)=\frac{\frac{I_m}{1+\gamma}\left[\gamma\left(\sin\beta+\frac{\sin 5\beta}{5}\right)+\left(\frac{2\cos\left(\frac{\alpha}{2}\right)\sin 3\beta}{3\left(\cos\left(\frac{\alpha}{2}\right)-1\right)}-\frac{2\sin\beta\cos^3\beta}{\cos\left(\frac{\alpha}{2}\right)-1}\right)\right]}{\beta+\frac{\sin 6\beta}{6}-\frac{1}{1+\gamma}\left(\gamma\left(\sin\beta+\frac{\sin 5\beta}{5}\right)-\left(\frac{2\sin\beta\cos^3\beta}{\cos\left(\frac{\alpha}{2}\right)-1}-\frac{2\cos\left(\frac{\alpha}{2}\right)\sin 3\beta}{3\left(\cos\left(\frac{\alpha}{2}\right)-1\right)}\right)\right)} \tag{7}$$

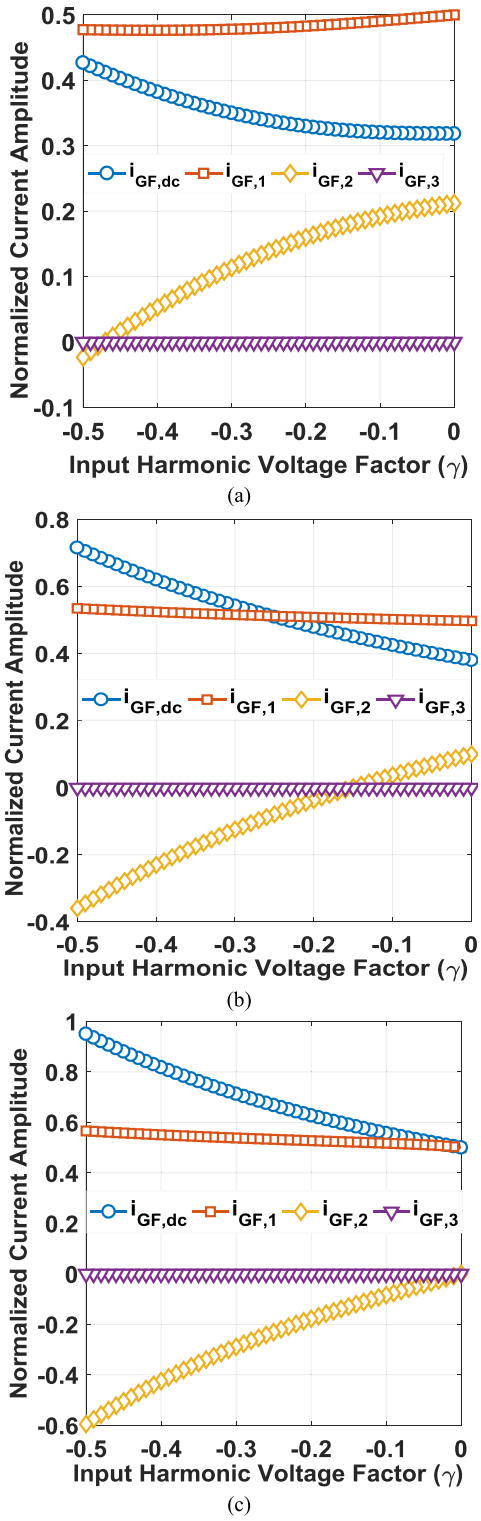

Fig. 7. Normalized intrinsic drain components. (a) Class GF for $\alpha = 180°$. (b) Class GF for $\alpha = 240°$. (c) Class GF $\alpha = f360°$.

drain waveforms impacting the current components. In practice, while controlling up to three harmonics, the drain voltage ($V_{\mathrm{GF}^{-1}}$) is shaped to half-sinusoidal as seen in Fig. 8 and is expressed as

$$V_{\mathrm{GF}^{-1}}(\theta) = \left(1 - \sqrt{2}\cos\theta + \frac{1}{2}\cos 2\theta\right). \tag{12}$$

Under class GF^{-1} PA operation the drain current can be formulated as a function of (γ), (α), (θ), and (I_m) and is given as

$$\begin{aligned} &i_{\mathrm{GF}^{-1}}(\theta, \alpha, \gamma, I_m) \\ &= I_m\left(\frac{\cos\theta - \cos\left(\frac{\alpha}{2}\right)}{1 - \cos\left(\frac{\alpha}{2}\right)} + \gamma\cos 2\theta\right) - i_{r2}(\alpha, \beta, \gamma, I_m)\cos 2\theta \\ &\quad -\beta(\alpha,\gamma) \le \theta \le \beta(\alpha,\gamma) \\ &\quad 0; \quad -\pi < \theta < -\beta(\alpha,\gamma), \beta(\alpha,\gamma) < \theta < \pi. \end{aligned} \tag{13}$$

The open circuit condition at second harmonic forces exclusion of second harmonic drain current ($i_{r2}(\alpha, \beta, \gamma, I_m)\cos 2\theta$), where $i_{r2}(\alpha, \beta, \gamma, I_m)$, the real part of second harmonic drain current, can be computed by imposing boundary condition in (14) and is given by (15), shown at the bottom of the next page,

$$\frac{1}{\pi}\int_{-\beta(\alpha,\gamma)}^{\beta(\alpha,\gamma)} i_{\mathrm{GF}^{-1}}(\theta, \alpha, \gamma, I_m)\cdot\cos 2\theta d\theta = 0. \tag{14}$$

Applying the Fourier series expansion of $i_{\mathrm{GF}^{-1}}$ given by (12), the dc ($i_{\mathrm{GF}^{-1},\mathrm{dc}}$), fundamental ($i_{\mathrm{GF}^{-1},1}$), second ($i_{\mathrm{GF}^{-1},2}$), third ($i_{\mathrm{GF}^{-1},3}$) harmonic drain current components can be evaluated by as

$$\begin{aligned} &i_{\mathrm{GF}^{-1},\mathrm{dc}}(\alpha, \beta, \gamma, I_m) \\ &= \frac{I_m}{2\pi}\left(\gamma\sin 2\beta + \frac{2\left(\beta\cos\left(\frac{\alpha}{2}\right) - \sin\beta\right)}{\cos\left(\frac{\alpha}{2}\right) - 1}\right) \\ &\frac{-i_{r2}(\alpha, \beta, \gamma, I_m)\sin 2\beta}{2\pi} \end{aligned} \tag{16}$$

$$\begin{aligned} &i_{\mathrm{GF}^{-1},1}(\alpha, \beta, \gamma, I_m) \\ &= \frac{(I_m\gamma - i_{r2}(\alpha, \beta, \gamma, I_m))\left(2\sin\beta - \frac{4}{3}\sin^3\beta\right)}{\pi} \\ &\quad + \frac{I_m}{\pi}\left(\frac{2\cos\left(\frac{\alpha}{2}\right)\sin\beta - \beta - \frac{\sin 2\beta}{2}}{\cos\left(\frac{\alpha}{2}\right) - 1}\right) \end{aligned} \tag{17}$$

$$\begin{aligned} &i_{\mathrm{GF}^{-1},2}(\alpha, \beta, \gamma, I_m) \\ &= \frac{(I_m\gamma - i_{r2}(\alpha, \beta, \gamma, I_m))\left(\beta + \frac{\sin 4\beta}{4}\right)}{\pi} \\ &\quad + \frac{I_m}{\pi}\left(\frac{\cos\left(\frac{\alpha}{2}\right)\sin 2\beta - 2\sin\beta + \frac{4}{3}\sin^3\beta}{\cos\left(\frac{\alpha}{2}\right) - 1}\right) \end{aligned} \tag{18}$$

$$\begin{aligned} &i_{\mathrm{GF}^{-1},3}(\alpha, \beta, \gamma, I_m) \\ &= \frac{(I_m\gamma - i_{r2}(\alpha, \beta, \gamma, I_m))\left(\sin\beta + \frac{\sin 5\beta}{5}\right)}{\pi} \\ &\quad + \frac{I_m}{3\pi}\left(\frac{2\ \sin 3\beta\cos\frac{\alpha}{2} - 6\sin\beta\cos^3\beta}{\cos\left(\frac{\alpha}{2}\right) - 1}\right). \end{aligned} \tag{19}$$

As seen in Fig. 9, the change in dc and fundamental current components are relatively insignificant compared to class GF PA mode. The effect of the second harmonic nonlinear component generated at the input is diminished because of the presence of infinite second harmonic impedance at the drain of the device. The open circuit impedance at second harmonic load traps second harmonic components that the device attempts to generate. Therefore, the class GF^{-1}PA

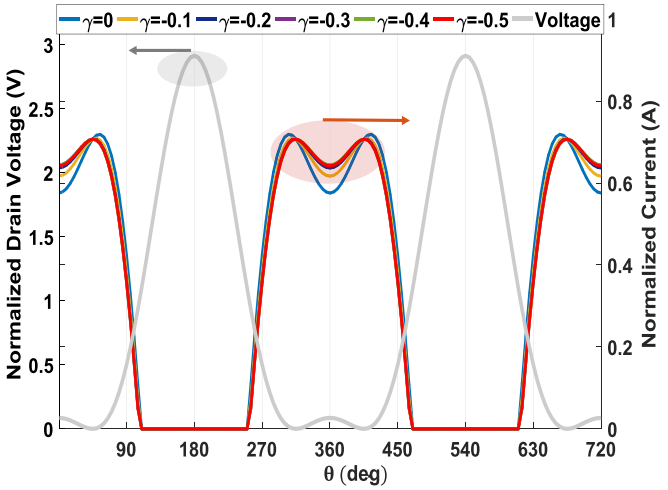

Fig. 8. Class GF^{-1} drain voltage and current waveforms as a function of γ for class B ($\alpha = 180°$).

current waveforms remain unaltered even with the input nonlinearity as seen in Fig. 8. In the design of high-efficiency PA, the load terminations are often considered as standalone without studying interaction of these load impedances with the terminations at the source. This analysis is indeed very important to understand the dependence of the source and load harmonic impedances on each other in the design of high-efficiency PAs. For $\gamma = 0$, $i_{GF^{-1},dc} = 1/\pi$, $i_{GF^{-1},1} = (1/2 - 8/9\pi^2)$, $i_{GF^{-1},2} = 0$, and $i_{GF^{-1},3} = -8/5\pi^2$ which are current components of a square current waveform in class F^{-1} PA as seen in Fig. 9(a) and the same as given in [5], [24], [25].

C. Theoretical Performance and Design Space

The drain currents extracted in Section III can be used to evaluate the theoretically achievable efficiency in case of class GF/class GF^{-1}PA. The generalized output power and DE for class GF and class GF^{-1} can be readily computed as a function of device knee voltage (V_k) and the drain bias voltage (V_{dc}) using (4)–(9), (12)–(17) as

$$\eta_{GF} = \frac{P_{out\_GF}}{P_{dc\_GF}} = \frac{\frac{1}{\sqrt{3}}\left(1 - \frac{V_k}{V_{dc}}\right) i_{GF,1}(\theta, \alpha, \gamma, I_m)}{i_{GF,dc}(\theta, \alpha, \gamma, I_m)} \quad (20)$$

$$\eta_{GF^{-1}} = \frac{P_{out\_GF^{-1}}}{P_{dc\_GF^{-1}}} = \frac{\frac{1}{\sqrt{2}}\left(1 - \frac{V_k}{V_{dc}}\right) i_{GF^{-1},1}(\theta, \alpha, \gamma, I_m)}{i_{GF^{-1},dc}(\theta, \alpha, \gamma, I_m)}. \quad (21)$$

In practice, this efficiency varies as a function of γ, which also corresponds to the second harmonic source impedance termination. Using (20) and (21), theoretical DE can be plotted with change in γ as shown in Fig. 10. As seen in Fig. 10(a), for class GF amplifiers the DE decreases function of γ. For $\gamma = 0$,

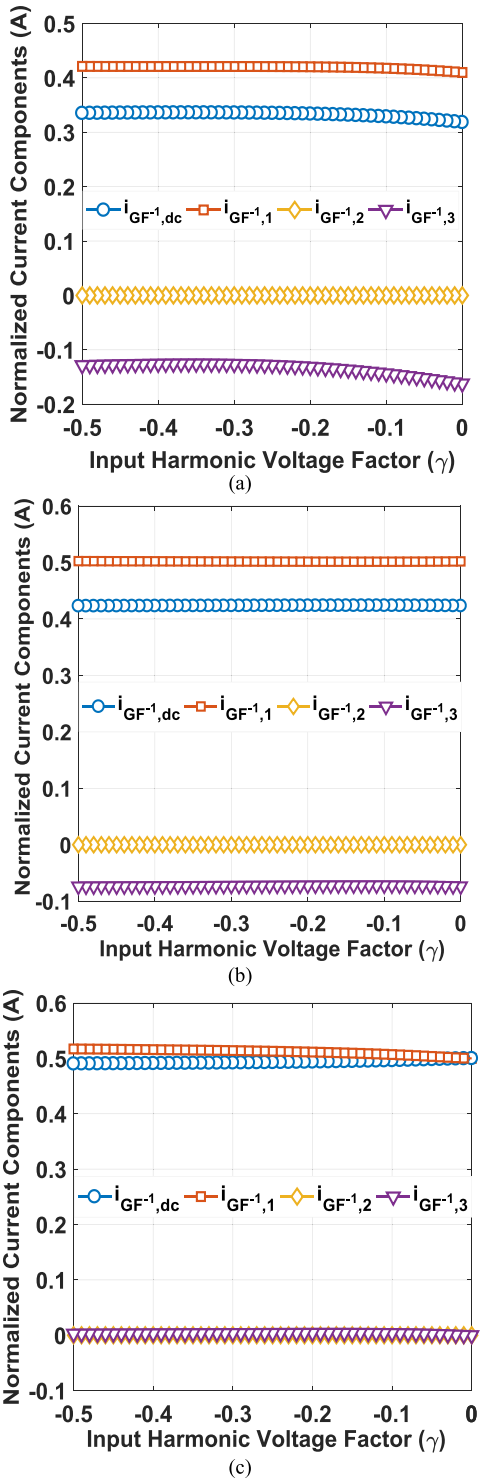

Fig. 9. Normalized intrinsic drain components. (a) Class $GF^{-1}\alpha = 180°$. (b) Class $GF^{-1}\alpha = 240°$. (c) Class $GF^{-1}\alpha = 360°$.

class GF and class GF^{-1} amplifiers can theoretically achieve a maximum efficiency of 90.6% and 91.07%, respectively which is exactly the same as class F and class F^{-1} PA [22], [25].

$$i_{r2}(\alpha, \beta, \gamma, I_m) = I_m \left(\frac{\gamma \left(\beta + \frac{\sin 4\beta}{4}\right)\left(\cos\left(\frac{\alpha}{2}\right) - 1\right) + \cos\left(\frac{\alpha}{2}\right)\sin 2\beta - \left(2\sin\beta - \frac{4}{3}\sin^3\beta\right)}{\left(\cos\left(\frac{\alpha}{2}\right) - 1\right)\left(\beta + \frac{\sin 4\beta}{4}\right)} \right) \quad (15)$$

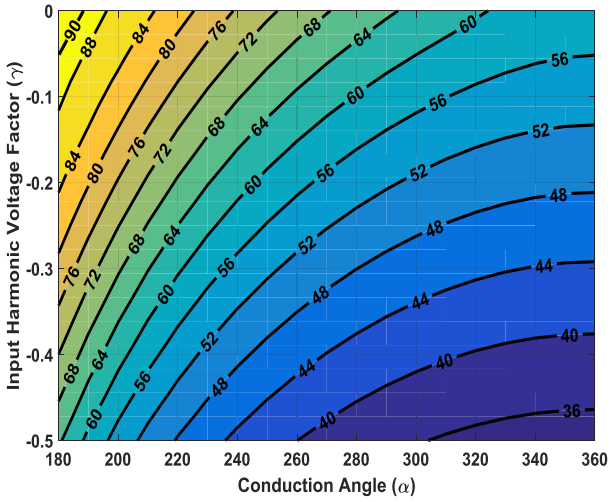

(a)

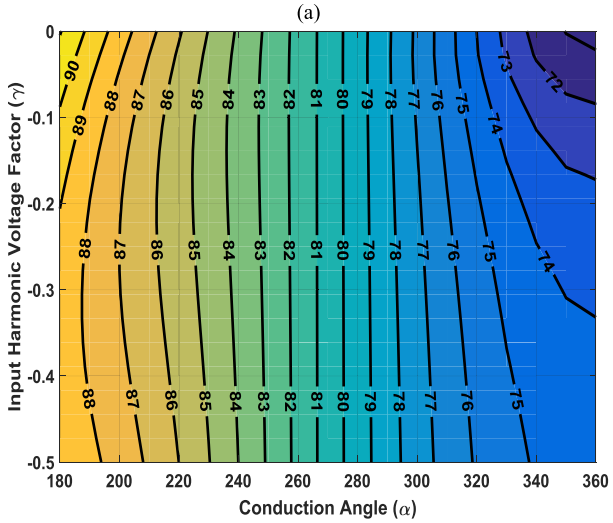

(b)

Fig. 10. Theoretical DE as a function of γ and α. (a) Class GF. (b) Class GF^{-1}.

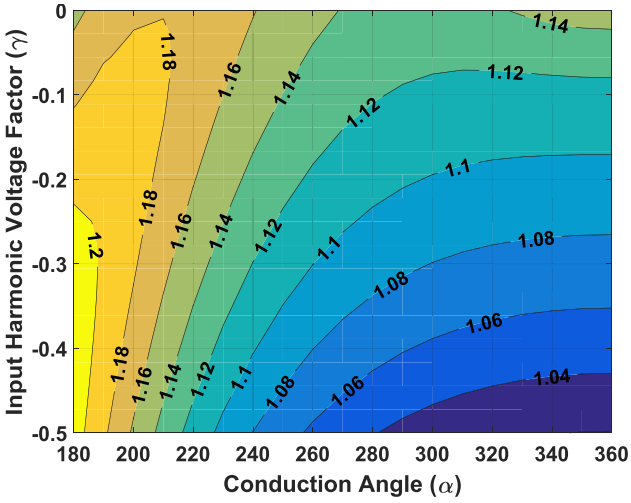

(a)

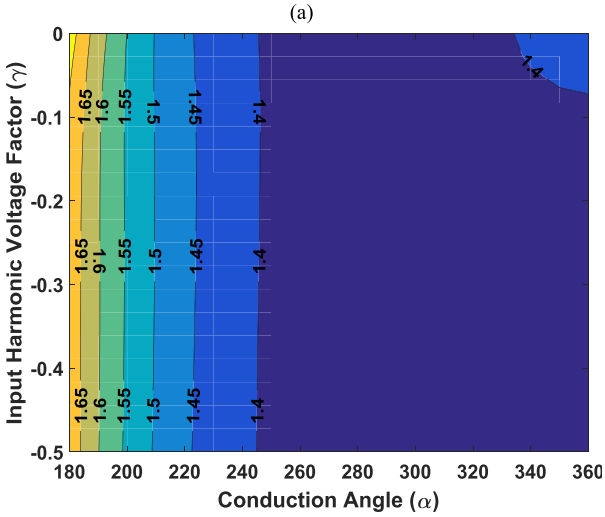

(b)

Fig. 11. Normalized fundamental impedance as a function of γ and α. (a) Class GF. (b) Class GF^{-1}.

For $\alpha = 180°$, theoretical degradation of 15%–20% occurs for the class GF amplifier with variation in γ. However, in practical scenarios, the generation of this second harmonic content relative to fundamental is limited by device periphery and technology. This theoretical DE is thus limited to 8%–10% which is reported in later sections. In contrast, class GF^{-1} amplifiers show almost no DE degradation with change in γ for class B to almost class A mode of opearation range. For this range and for specific α, the change in DE is less than 2%. Under class GF^{-1} PA operation, the load harmonic conditions offer significant immunity to any variation in γ. An open circuit condition at load does not allow any second harmonic input nonlinearity to impact the waveforms and drain current components thereby maintaining the same theoretical DE.

However, the input harmonic termination impacts the fundamental load design space for both class GF and class GF^{-1} PA operation. Using (4), (9), (12), and (17) the fundamental impedance can be computed as a function of class B load impedance $R_{\text{opt\_B}} = (V_{\text{dc}} - V_k)/(I_m/2)$ and is given by

$$Z_{1,\text{GF}} = \frac{I_m}{\sqrt{3} i_{\text{GF},1}(\theta, \alpha, \gamma, I_m)} R_{\text{opt\_B}} \tag{22}$$

$$Z_{1,\text{GF}^{-1}} = \frac{I_m}{\sqrt{2} i_{\text{GF}^{-1},1}(\theta, \alpha, \gamma, I_m)} R_{\text{opt\_B}}. \tag{23}$$

The class GF fundamental impedance map is shown in Fig. 11(a). $Z_{1,\text{GF}}$ varies from $R_{\text{opt\_B}}$ to 1.25 $R_{\text{opt\_B}}$ for different conduction angles. For $\alpha = 180°, \gamma = 0$, $Z_{1,\text{GF}} = 1.15\ R_{\text{opt\_B}}$ which is the same as fundamental impedance of class F PA [22], [27]. Similarly, class GF^{-1} impedance map shown in Fig. 11(b) shows variation in fundamental impedance from 1.72 $R_{\text{opt\_B}}$ to 1.67 $R_{\text{opt\_B}}$. For $\alpha = 180°$, $\gamma = 0$, $Z_{1,\text{GF}^{-1}} = 1.72\ R_{\text{opt\_B}}$ which is the same as fundamental impedance for conventional class F^{-1} PA [5], [24], [25].

IV. Experimental Validation

A. Intrinsic Waveform Analysis and Harmonic Source Pull

The initial validation of the proposed operation of class GF and class GF^{-1} is carried out using NXP 1.95-mm GaN die. As the theoretical analysis is focused on the intrinsic drain plane (current generator), the classes of operation are confirmed using the NXP GaN model with intrinsic node access. At a frequency of 2.6 GHz, an ideal class GF (α, $\gamma = 0$)

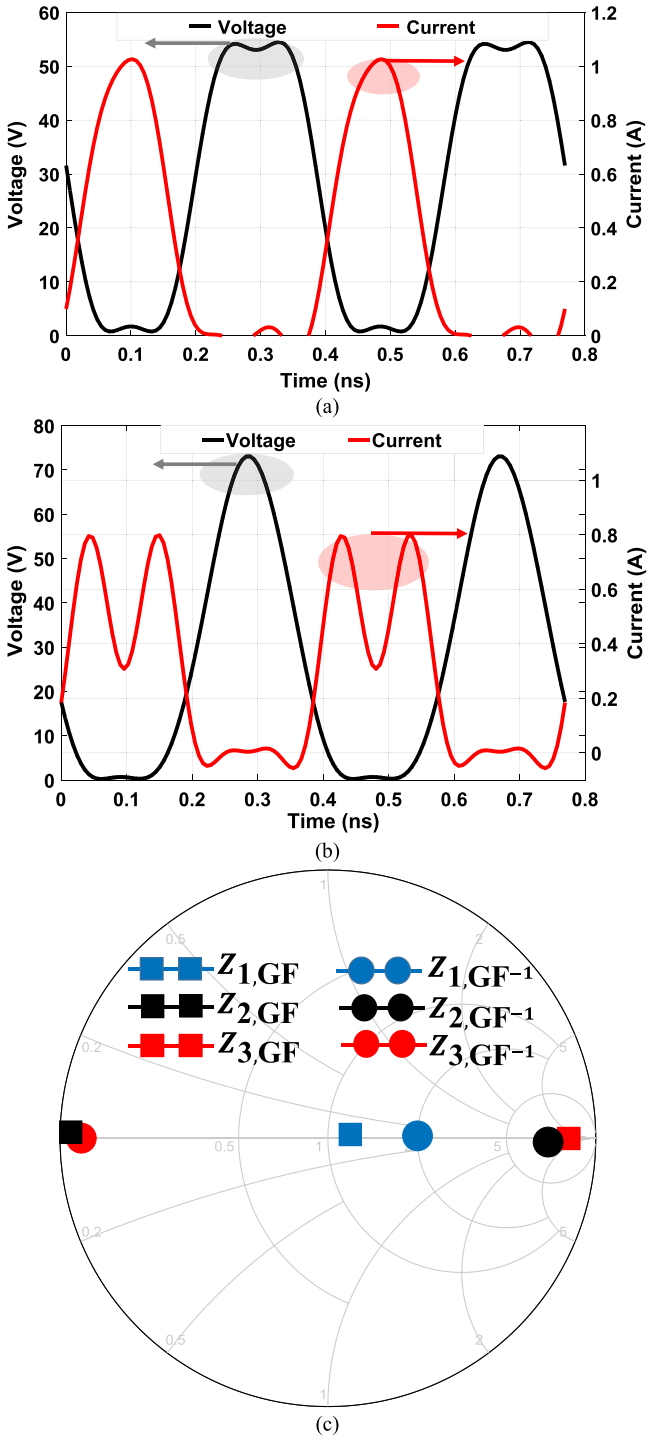

Fig. 12. Intrinsic drain voltage and current waveforms for (a) class GF loading conditions at $P_{in} = 17.5$ dBm. (b) Class GF^{-1} loading conditions at $P_{in} = 19$ dBm normalized with characteristic impedance of 50 Ω. (c) Intrinsic design space for class GF/GF^{-1} amplifiers.

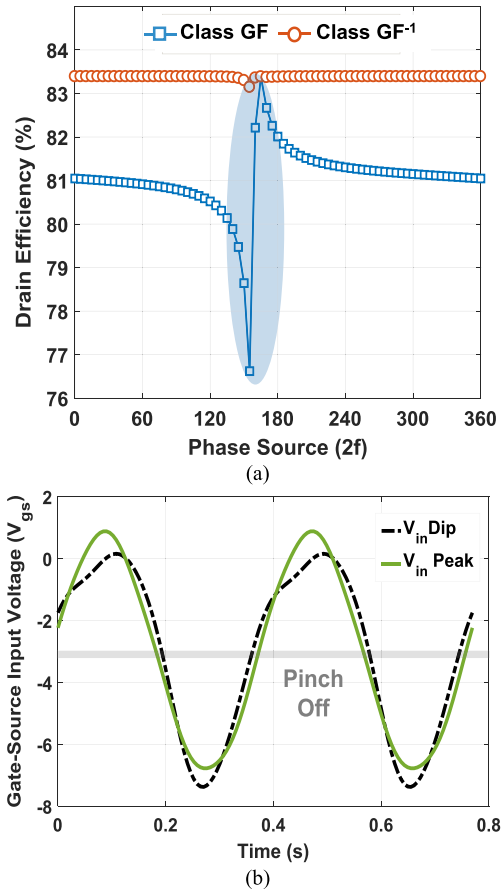

Fig. 13. (a) DE versus the phase of a second harmonic source for class F/class F^{-1} loading condition. (b) Input gate waveform for the maximum efficiency (V_{in} peak) and minimum efficiency (V_{in} dip) in class GF PA.

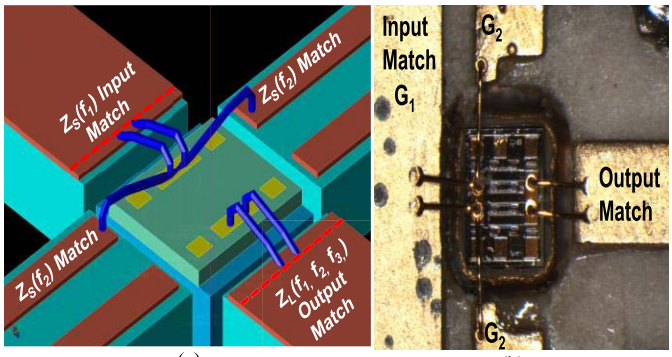

Fig. 14. (a) Bonding diagram for a realization of harmonic traps both at input and output of the device. (b) Photograph of the wire-bonded die to the PCB plane.

and an ideal class GF^{-1}(α, $\gamma = 0$) PA were analyzed using load pull at a 3-dB gain compression. As seen in Fig. 12(a), a square voltage and half-sinusoidal drain current waveform confirms class GF PA mode of operation. The de-embedded design space at current generator plane for class GF amplifier is shown in Fig. 12(c). Once the output loading conditions are fixed, a second harmonic source pull is performed. The DE varies as a function of second harmonic source phase for class GF loading condition causing an efficiency degradation of 7% as shown in Fig. 13(a). The results agree with theoretical efficiency derived in Section III-C.

Similarly, an ideal class GF^{-1} operation is confirmed by intrinsic waveform i.e., half-sinusoidal voltage and square current waveform shown in Fig. 12(b). Unlike the class GF, the efficiency of the class GF^{-1} amplifier remains constant

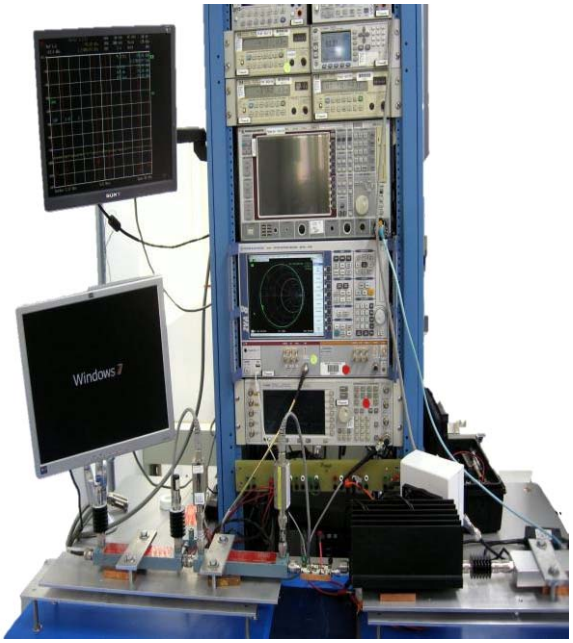

Fig. 15. Measurement bench setup up.

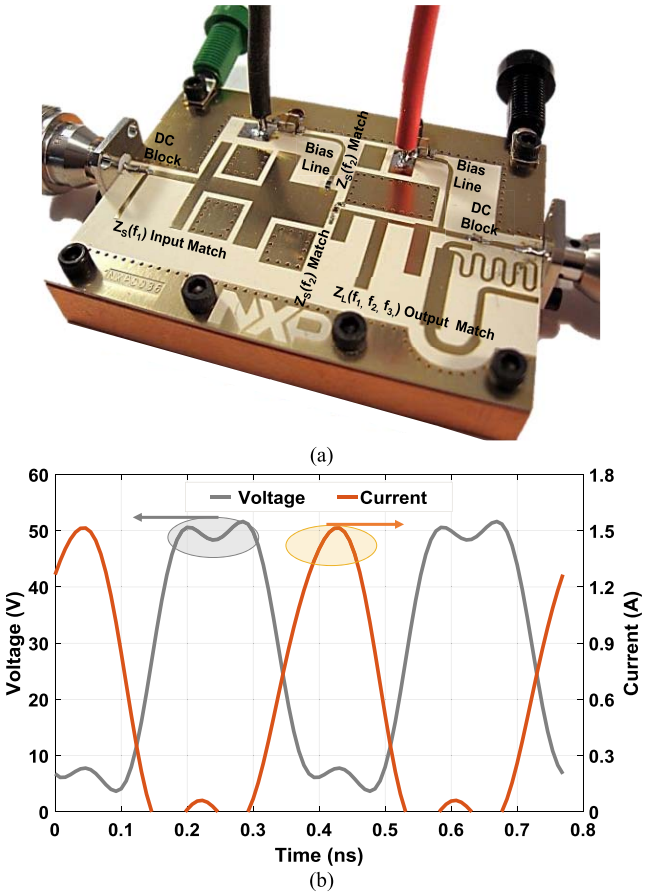

Fig. 16. (a) Fabricated class GF prototype. (b) Intrinsic drain square voltage and half-sinusoidal current waveforms of class GF at 2.6 GHz.

regardless of second harmonic source termination as can be inferred from Fig. 13(a). This result is also in agreement with theoretical derivation reported in Fig. 10(a) and 10(b).

The drop in efficiency for a second harmonic source–pull in class GF also confirms importance of input waveform shaping. An undesired area exists on some regions of Smith Chart for second harmonic source where efficiency degrades significantly. It is noteworthy that at the null of this region, $C_{\rm gs}$ generates extreme amplitude of second harmonic content which alters the shape of the sinusoidal waveform. The gate voltage waveforms for GaN die is extracted and depicted in Fig. 13(b). With the out-of-phase second harmonic component, the conduction angle increases resulting in loss of efficiency as explained in Section III-C. In fact, it implies that a class GF PA, when driven with this distorted waveform, experiences efficiency degradation. On contrary, no significant drop in efficiency is observed in case of class GF^{-1} amplifiers. The source terminations for class GF PA are more sensitive to any harmonic mismatch at the input and needs to be terminated in safer regions to avoid DE degradation.

B. PA Design and Fabrication

The experimental validation of the work is divided into two folds, one based on the load pull and other based on PA design and fabrication. The objective from load–pull was to confirm the immunity of second harmonic source for class GF^{-1} amplifiers which is described in detail in Section-IVA. For NXP 1.95 mm die, the intrinsic parasitics are extracted and used to embed harmonic impedances to bond wire or printed circuit board (PCB) reference plane. A finite electromagnetic (FEM) simulation-based model for bond wires including bond pads is generated using the preferred geometry for two wires landing on the die pad. The device is stabilized using a parallel *RC* network at the input side. This FEM bond wire model along with the input stability network is used to evaluate the source impedance, which is conjugate matched to the input impedance seen by the device. After fixing the fundamental source impedance with fixed harmonic loading condition, the fundamental load–pull is performed by sweeping the power levels until 3-dB gain compression is reached. For class GF and GF^{-1} output loading conditions, the fundamental impedance for maximum efficiency and maximum power is then identified. With optimized terminations at the load an input second harmonic source–pull is done. With a selected second harmonic source termination for maximum efficiency at P3 dB, a refundamental source–pull is carried out to study impact of $Z_{\rm 2fsource}$ on fundamental source impedance. This iterative source– and load–pull helps in best optimizing of performance at P3dB compression limit. Once the impedances are determined, a low pass topology using distributed structures is used for designing the output matching network, which also include dual-gate series *LC* resonance circuit to control the second harmonic source impedance. The matching networks of the class GF, class GF^{-1} PAs were realized on a low loss 20-mil PCB substrate with permittivity of 3.6. NXP active GaN die with gate periphery of 1.95 mm is mounted directly on the copper heat sink and wire bonded to the PCB as seen in Fig. 14 (a) and (b). The PAs are stabilized using a parallel combination of *RC* network at the input

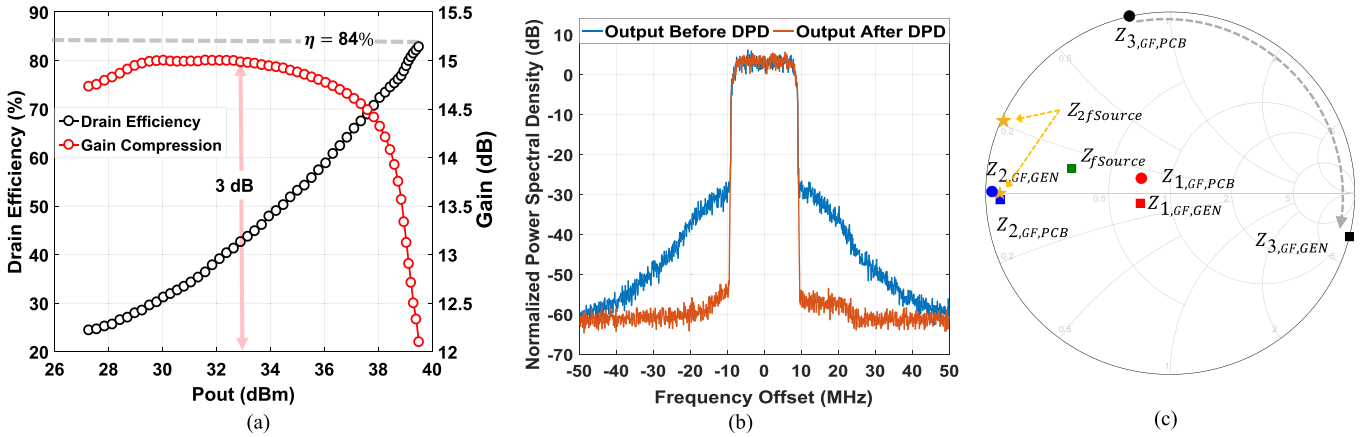

Fig. 17. Class GF mode of Operation. (a) Measured gain and DE versus output power at frequency of 2.6 GHz for $Z_{2\text{fsource}}$ = short. (b) Output spectrum before and after DPD. (c) De-embedded intrinsic impedances at the current generator plane of GaN 1.95-mm device.

with values of 21 Ω and 6 pF, respectively for frequencies ranging from baseband up to third harmonic. For accurate measurements, the RF bench is used. The measurement setup is shown in Fig. 15 essentially consists of Rhode and Schwarz SMU200A modulated signal source which drives the DUT through 50-W Amplifier Research AR driver with linear gain >45 dB. The isolator is placed at the driver output to provide fixed 50-Ω source impedance to the DUT and hence prevent any standing waves caused due to the mismatch between the driver and the DUT input. Effective input and output power of the DUT, coupled through the directional couplers, are measured using Keysight N1912B power meters with over 60-dB dynamic range capability. Rhode and Schwartz Spectrum Analyzer FSQ8 is also incorporated in the setup to compute ACPR from the captured PA output spectrum.

The PA implementation is carried out with four different second harmonic source ($Z_{2\text{fsource}}$) terminations for both class G_F and class GF^{-1} PA modes at carrier a frequency of 2.6 GHz. The measured performance for each individual case is presented in the following section. These results were compiled from measured data on a NXP GaN HEMT die using active load–pull system.

Design Case I) class GF with $Z_{2\text{fsource}}$ = *short:* class GF PA was realized by terminating the Z_{2L} and Z_{3L} along with a short $Z_{2\text{fsource}}$ termination which is realized on the PCB. If PAs are not terminated for second harmonic source ($Z_{2\text{fsource}}$), there is a risk of this impedance falling in the DE dip. To make sure the $Z_{2\text{fsource}}$ lies away from the dip, an *LC* resonance network using wire bond and capacitor is used to realize a short termination. The device was biased at a drain supply voltage of 28 V and bias quiescent current of 40 mA.

The PA prototype with a dimension of 30 mm × 30 mm is shown in Fig. 16(a). The intrinsic plane square voltage waveform and half-sinusoidal current waveforms confirms the class GF PA mode of operation as seen in Fig. 16(b). Under this configuration, the class GF PA exhibits a DE of 84% at an output power level of 39.9 dBm with a gain of 12 dB at P3 dB gain compression as seen in Fig. 17(a). The PA was tested with 1c-LTE 20-MHz signal with peak-to-average ratio of 7.2 dB. The closed-loop digital predistortion (DPD)

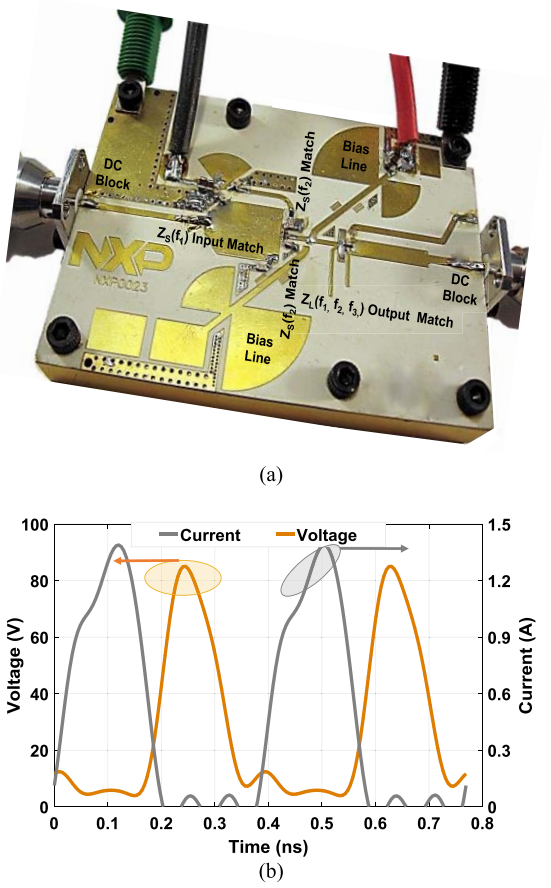

Fig. 18. (a) Fabricated class GF^{-1} prototype. (b) Intrinsic drain half-sine voltage and right side shaped current waveforms of class GF^{-1} at 2.6 GHz.

was accomplished using the NXP AFD-4400 DPD system. NXP's generalized memory polynomial-based DPD system is realized using vector signal processing accelerator–NXP's set to 307.2-MHz proprietary vector signal processors with a DPD sampling rate set to 307.2 MHz. At 2.6-GHz carrier frequency, an average DE of 42% is achieved at 32.4-dBm output power, the adjacent channel power ratio at 20-MHz offset is

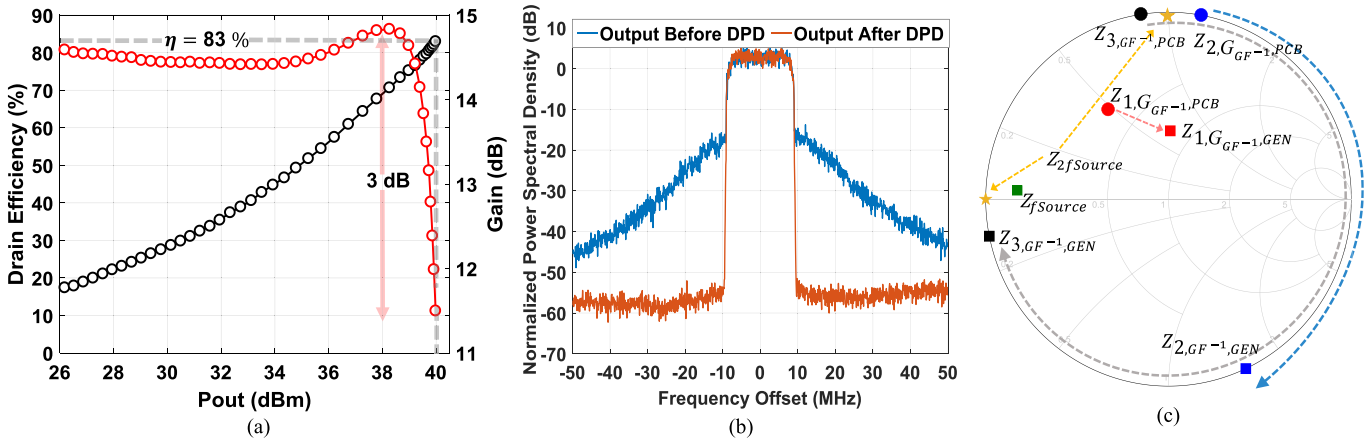

Fig. 19. Class GF^{-1} mode of operation. (a) Measured gain and DE versus output power at frequency of 2.6 GHz for $Z_{2fsource}$ = short. (b) Output spectrum before and after DPD (c) De-embedded intrinsic impedances at the current generator plane of GaN 1.95-mm device.

improved to −60 dB after DPD as shown in Fig. 17(b). The de-embedded intrinsic impedances are shown in Fig. 17(c), where the second harmonic impedance at current generator plane ($Z_{2,\ GF,\ GEN}$) is short and third harmonic impedance at the current generator plane ($Z_{3,GF,\ GEN}$) is at open circuit.

Design Case II) class GF^{-1} *with* $Z_{2fsource}$ = *short:* class GF^{-1} is implemented by realizing a short $Z_{2fsource}$ impedance. The GaN 1.95 mm die was biased at a quiescent current of 40 mA, with the drain–source voltage of 28 V. The fabricated PA prototype is shown in Fig. 18(a), with intrinsic current and voltage waveforms in Fig. 18(b). The drain voltage is shaped as rectified half-sinusoidal with a total swing of $3 \times V_{dd}$ confirming class GF^{-1} PA operation. The PA exhibits DE of 83% with an output power of 40 dBm and gain of 12 dB at P3 dB gain compression when as shown in Fig. 19(a). At 2.6-GHz carrier frequency, an average DE of 40% is achieved at 32.6-dBm output power, the adjacent channel power ratio at 10-MHz offset is improved to −55 dB after DPD as presented in Fig. 19(b). The de-embedded design space at intrinsic plane $Z_{2,\ GF^{-1},\ GEN}$ and $Z_{3,\ GF^{-1},\ GEN}$ is shown in Fig. 19(c). The PA is optimized for 3-dB compression limit where a reactive second harmonic helps in right side shaping of the current waveform [28].

Design Case III) class GF with $Z_{2fsource} = j10\ \Omega$*:* to study the impact of input nonlinearity on the class GF PA, the input second harmonic termination is shifted changing the capacitance of the source *LC* resonance circuit. For a second harmonic source termination of $j10\ \Omega$, class GF PA exhibits measured DE of 76% with an output power of 39.8 dBm and gain of 13 dB as shown in Fig. 20(a). This corresponds to a degradation 6% compared to the Design case I where the second harmonic source is tuned to short. As explained in Sections III-C and IV-A, the DE degrades because of selection of second harmonic source in the dip region.

Design Case IV) class GF^{-1} *with* $Z_{2fsource} = j50\ \Omega$*:* to confirm the immunity of second harmonic source mismatch in case of $Z_{2fsource}$ is terminated by $j50\ \Omega$. Under this configuration, the PA achieves a measured DE of 82% with 39.9 dBm output power at 3-dB gain compression as shown in Fig. 20(b). The achieved performance is similar design

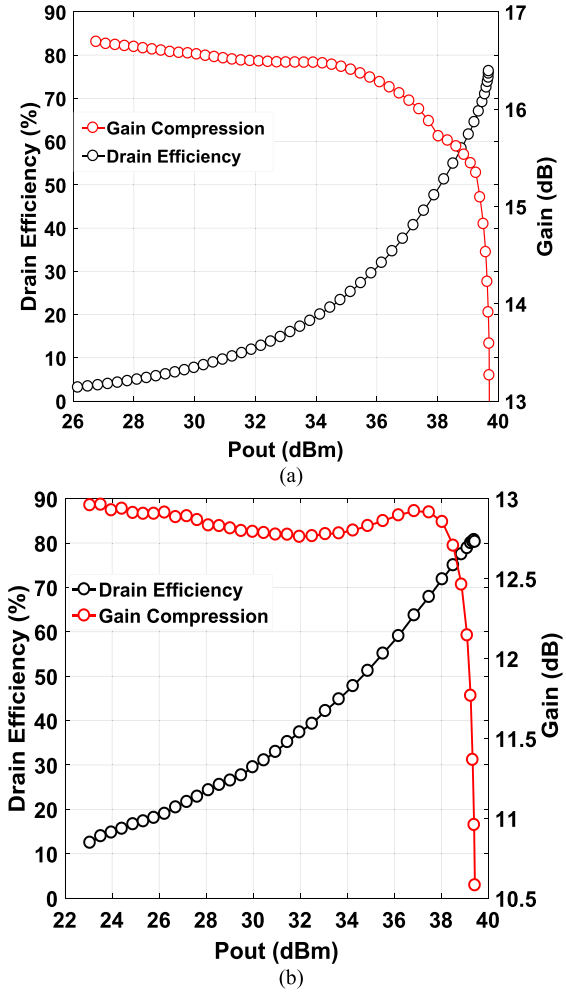

Fig. 20. Measured gain and DE versus output power at a frequency of 2.6 GHz. (a) Class GF PA for $Z_{2fsource}$ of j10 Ω. (b) Class GF^{-1}PA for $Z_{2fsource}$ of j50 Ω.

case (III) of class GF^{-1}PA, thereby confirming the theoretical prediction reported in Section III-C.

Furthermore, the obtained results were benchmarked against the existing works in high-efficiency HT PA design. The comparison is reported in Table I where the performance

TABLE I
PERFORMANCE COMPARISON WITH STATE-OF-THE-ART HIGH-EFFICIENCY PAs

Ref	f (GHz)	P_{out} (W)	DE (%)	PAE (%)	FE (%)	Class
[29]	2.14	20	73.7	70	84.6	E
[30]	2.65	47.9	71.5	66	84.2	Sat
[31]	3.54	55	70	63	86.4	F^{-1}
		52.5	69.4	62.4	85.5	F
[32]	2.1	11.9	81	78.2	94.0	F^{-1}
[33]	0.3	17	81	76.58	56.6	F
		17.25	79	73	54.0	F^{-1}
[34]	2.14	11.5	73.5	70	84.7	F^{-1}
[35]	1	9.0	83.1	81.3	81.3	F^{-1}
[36]	1.5	15	85	81	89.9	FHP
	2.2	9	91	80	97.4	THP
[37]	2.65	11	78	75.1	95.9	Sat
This Work	2.6	9.8	84	78.7	99.0	GF $Z_{2fsource}$=0
		9.5	76	72.6	92.2	GF $Z_{2fsource}$=j10Ω
		10	83	77.0	97.7	GF^{-1} $Z_{2fsource}$=0
		9.8	82	75	95.0	GF^{-1} $Z_{2fsource}$=j50 Ω

f: Frequency, DE: drain efficiency, $P_{out:}$ output power, PAE: Power added efficiency, FE: frequency weighted efficiency $(GHz)^{0.25}$ x PAE, FHP: Fifth Harmonic Peaking, THP: Third harmonic peaking.

of this PA in terms of PAE and frequency weighted efficiency [27] is among the very best.

V. CONCLUSION

Generalized HT amplifiers denoted as class GF and class GF^{-1} PA was presented in this paper. The generalized theory considers the impact of input nonlinearity and supports any conduction angle for different output harmonic conditions. It has been observed that class GF and class GF^{-1} PA modes react differently to input nonlinearity, which is controlled by the second harmonic impedance at the input of the device. The performance of class GF^{-1} is immune to any change in second harmonic impedance at the input of the device thereby offering a design advantage in selection of second harmonic source impedance. It is also proved that second harmonic current in class GF^{-1} and third harmonic current in class GF diminishes to zero for any second harmonic condition at input of the device. These findings are validated using NXP 1.95-mm GaN die. Several PAs were designed for different input harmonic terminations and some of the prototypes achieve one of the very best frequency weighted efficiency of 99% and 97.7% for class GF and Class GF^{-1}, respectively.

ACKNOWLEDGMENT

The authors would like to thank Advanced Design team, RF power group at NXP Semiconductors, Chandler, AZ, USA, for support and advice.

REFERENCES

[1] *IMT Vision—Framework and Overall Objectives of the Future Development of IMT for 2020 and Beyond*, Doc. ITU-R M.2083-0, 2015.

[2] S. C. Cripps, *RF Power Amplifiers for Wireless Communications*, 2nd ed. Boston, MA, USA: Artech House, 2006.

[3] P. Colantonio, F. Giannini, and E. Limiti, *High Efficiency RF and Microwave Solid State Power Amplifiers*. New York, NY, USA: Wiley, 2009.

[4] Y. Y. Woo, Y. Yang, and B. Kim, "Analysis and experiments for high-efficiency class-F and inverse class-F power amplifiers," *IEEE Trans. Microw. Theory Techn.*, vol. 54, no. 5, pp. 1969–1974, May 2006.

[5] J. H. Kim, S. J. Lee, B. H. Park, S. H. Jang, J. H. Jung, and C. S. Park, "Analysis of high-efficiency power amplifier using second harmonic manipulation: Inverse class-F/J amplifiers," *IEEE Trans. Microw. Theory Techn.*, vol. 59, no. 8, pp. 2024–2036, Aug. 2011.

[6] F. H. Raab, "Maximum efficiency and output of class-F power amplifiers," *IEEE Trans. Microw. Theory Techn.*, vol. 49, no. 6, pp. 1162–1166, Jun. 2001.

[7] V. Vadalà, A. Raffo, S. Di Falco, G. Bosi, A. Nalli, and G. Vannini, "A load–pull characterization technique accounting for harmonic tuning," *IEEE Trans. Microw. Theory Techn.*, vol. 61, no. 7, pp. 2695–2704, Jul. 2013.

[8] P. Colantonio, F. Giannini, G. Leuzzi, and E. Limiti, "Theoretical facet and experimental results of harmonic tuned PAs," *Int. J. RF Microw. Comput.-Aided Eng.*, vol. 13, no. 6, pp. 459–472, Nov. 2003.

[9] P. Colantonio, F. Giannini, G. Leuzzi, and E. Limiti, "On the class-F power amplifier design," *Int. J. RF Microw. Comput.-Aided Eng.*, vol. 9, pp. 129–149, Mar. 1999.

[10] P. M. White, "Effect of input harmonic terminations on high efficiency class-B and class-F operation of PHEMT devices," in *IEEE MTT-S Int. Microw. Symp. Dig.*, Jun. 1998, pp. 1611–1614.

[11] K.-I. Jeon, Y.-S. Kwon, and S.-C. Hong, "Input harmonics control using non-linear capacitor in GaAs FET power amplifier," in *IEEE MTT-S Int. Microw. Symp. Dig.*, Jun. 1997, pp. 817–820.

[12] T. Canning, P. Tasker, and S. Cripps, "Waveform evidence of gate harmonic short circuit benefits for high efficiency X-band power amplifiers," *IEEE Microw. Wireless Compon. Lett.*, vol. 23, no. 8, pp. 439–441, Aug. 2013.

[13] D. Y.-T. Wu and S. Boumaiza, "Comprehensive first-pass design methodology for high efficiency mode power amplifier [TC contests]," *IEEE Microw. Mag.*, vol. 11, no. 1, pp. 116–121, Feb. 2010.

[14] M. Haynes, S. C. Cripps, J. Benedikt, and P. J. Tasker, "PAE improvement using 2nd harmonic source injection at X-band," in *Proc. Workshop Integr. Nonlinear Microw. Millim.-Wave Circuits (INMMIC)*, Sep. 2012, pp. 3–4.

[15] M. Haynes, P. J. Tasker, and S. C. Cripps, "High efficiency PA design strategy at X-band," in *Proc. IEEE Compound Semiconductor Integr. Circuit Symp. (CSICS)*, Monterey, CA, USA, Oct. 2013, pp. 1–4.

[16] A. Alizadeh, M. Frounchi, and A. Medi, "Waveform engineering at gate node of class-J power amplifiers," *IEEE Trans. Microw. Theory Techn.*, vol. 65, no. 7, pp. 2409–2417, Jul. 2017, doi: 10.1109/TMTT.2017.2651814.

[17] G. Bosi, A. Raffo, G. Vannini, E. Cipriani, P. Colantonio, and F. Giannini, "Gate waveform effects on high-efficiency PA design: An experimental validation," in *Proc. 9th Eur. Microw. Integr. Circuit Conf.*, Oct. 2014, pp. 329–332.

[18] J. J. Bussgang, L. Ehrman, and J. W. Graham, "Analysis of nonlinear systems with multiple inputs," *Proc. IEEE*, vol. 62, no. 8, pp. 1088–1119, Aug. 1974.

[19] P. Colantonio, F. Giannini, G. Leuzzi, and E. Limiti, "Multiharmonic manipulation for highly efficient microwave power amplifiers," *Int. J. RF Microw. Comput.-Aided Eng.*, vol. 11, no. 6, pp. 366–384, 2001.

[20] S. Jee *et al.*, "Asymmetric broadband Doherty power amplifier using GaN MMIC for femto-cell base-station," *IEEE Trans. Microw. Theory Techn.*, vol. 63, no. 9, pp. 2802–2810, Sep. 2015.

[21] B. M. Merrick, J. B. King, and T. J. Brazil, "The continuous harmonic-tuned power amplifier," *IEEE Microw. Wireless Compon. Lett.*, vol. 25, no. 11, pp. 736–738, Nov. 2015.

[22] T. Sharma, R. Darraji, F. Ghannouchi, and N. Dawar, "Generalized continuous class-F harmonic tuned power amplifiers," *IEEE Microw. Wireless Compon. Lett.*, vol. 26, no. 3, pp. 213–215, Mar. 2016.

[23] T. Sharma, R. Darraji, and F. Ghannouchi, "Design methodology of high-efficiency contiguous mode harmonically tuned power amplifiers," in *Proc. IEEE Radio Wireless Symp. (RWS)*, Austin, TX, USA, Jan. 2016, pp. 148–150.

[24] T. Sharma, R. Darraji, P. Mousavi, and F. M. Ghannouchi, "Generalized design of continuous-mode second harmonic tuned amplifiers," *Microw. Opt. Technol. Lett.*, vol. 58, pp. 2787–2789, Dec. 2016.

[25] T. Sharma, R. Darraji, and F. Ghannouchi, "A methodology for implementation of high-efficiency broadband power amplifiers with second-harmonic manipulation," *IEEE Trans. Circuits Syst. II, Exp. Briefs*, vol. 63, no. 1, pp. 54–58, Jan. 2016.
[26] P. Colantonio, F. Giannini, E. Limiti, and V. Teppati, "An approach to harmonic load– and source–pull measurements for high-efficiency PA design," *IEEE Trans. Microw. Theory Techn.*, vol. 52, no. 1, pp. 191–198, Jan. 2004.
[27] K. Chen and D. Peroulis, "Design of broadband highly efficient harmonic-tuned power amplifier using in-band continuous class-F^{-1}/F mode transferring," *IEEE Trans. Microw. Theory Techn.*, vol. 60, no. 12, pp. 4107–4116, Dec. 2012.
[28] T. Sharma, R. S. Embar, D. Holmes, R. Darraji, J. Jones, and F. Ghannouchi, "Harmonically engineered and efficiency enhanced power amplifier design for P3dB/backoff applications," in *IEEE MTT-S Int. Microw. Symp. Dig.*, Honolulu, HI, USA, 2017, 789–792, doi: 10.1109/MWSYM.2017.8058696.
[29] Y.-S. Lee and Y.-H. Jeong, "A high-efficiency class-E GaN HEMT power amplifier for WCDMA applications," *IEEE Microw. Wireless Compon. Lett.*, vol. 17, no. 8, pp. 622–624, Aug. 2007.
[30] J. Kim, J. Moon, J. Kim, S. Boumaiza, and B. Kim, "A novel design method of highly efficient saturated power amplifier based on self-generated harmonic current," in *Proc. Eur. Microw. Conf.*, Sep./Oct. 2009, pp. 1082–1085.
[31] J. H. Kim, G. D. Jo, J. H. Oh, Y. H. Kim, K. C. Lee, and J. H. Jung, "Modeling and design methodology of high-efficiency class-F and class-F^{-1} power amplifiers," *IEEE Trans. Microw. Theory Techn.*, vol. 59, no. 1, pp. 153–165, Jan. 2011.
[32] P. Wright, A. Sheikh, C. Roff, P. J. Tasker, and J. Benedikt, "Highly efficient operation modes in GaN power transistors delivering upwards of 81% efficiency and 12 W output power," in *IEEE MTT-S Int. Microw. Symp. Dig.*, Jun. 2008, pp. 1147–1150.
[33] R. A. Beltran, "Class-F and inverse class-F power amplifier loading networks design based upon transmission zeros," in *IEEE MTT-S Int. Microw. Symp. Dig.*, Tampa, FL, USA, Jun. 2014, pp. 1–4.
[34] S. Hong *et al.*, "High efficiency GaN HEMT power amplifier optimized for OFDM EER transmitter," in *IEEE MTT-S Int. Microw. Symp. Dig.*, Jun. 2007, pp. 1247–1250.
[35] M. Helaoui and F. M. Ghannouchi, "Optimizing losses in distributed multiharmonic matching networks applied to the design of an RF GaN power amplifier with higher than 80% power-added efficiency," *IEEE Trans. Microw. Theory Techn.*, vol. 57, no. 2, pp. 314–322, Feb. 2009.
[36] M. Thian, A. Barakat, and V. Fusco, "High-efficiency harmonic-peaking class-EF power amplifiers with enhanced maximum operating frequency," *IEEE Trans. Microw. Theory Techn.*, vol. 63, no. 2, pp. 659–671, Feb. 2015.
[37] J. Kim *et al.*, "Saturated power amplifier optimized for efficiency using self-generated harmonic current and voltage," *IEEE Trans. Microw. Theory Techn.*, vol. 59, no. 8, pp. 2049–2058, Aug. 2011.

Tushar Sharma (M'10) received the B.Tech. degree in electronics and communications engineering from Guru Gobind Singh Indraprastha University, Delhi, India. He is currently pursuing the Ph.D. degree at the University of Calgary, Calgary, AB, Canada.

From 2016 to 2017, he was a Research and Development Design Intern with NXP Semiconductors, Chandler, AZ, USA. He has authored or co-authored over 16 refereed publications. His current research interests include high-efficiency broadband RF power amplifiers, waveform engineering techniques for power amplifiers, and active/passive load–pull techniques.

Mr. Sharma was a recipient of the Izaak Walton Killam Pre-Doctoral Scholarship, the AITF Doctoral Scholarship, the Alberta Transformative Talent scholarship, the Academic Excellence Award, and the Research Productivity Award.

Srinidhi E. R. received the M.Sc. and Ph.D. degrees from the University of Kassel, Kassel, Germany, in 2005 and 2009, respectively.

He is currently a Senior RF Design Engineer with the RF Group, NXP Semiconductors Inc., Chandler, AZ, USA. He has authored or co-authored over 20 publications in international journals and conference proceedings and holds 12 U.S. patents with 4 pending. His current research interests include the design of high-efficiency microwave power amplifiers and digital predistortion for cellular base-station infrastructures.

Ramzi Darraji (S'10–M'13) received the M.Sc. degree in communications engineering from the École Supérieure des Communications de Tunis, Ariana, Tunisia, in 2008, and the Ph.D. degree in electrical engineering from the University of Calgary, Calgary, AB, Canada, in 2013.

He is currently with Syntronic Research and Development Canada Inc., Kanata, ON, Canada. He has authored or co-authored over 30 refereed publications and has 4 patent applications. His current research interests include high-efficiency power amplifiers' design for cellular applications and advanced RF front-end solutions for fifth-generation communication systems.

Damon G. Holmes (M'13) received the B.Sc. and M.Sc. degrees from the University of Calgary, Calgary, AB, Canada, in 2002 and 2005, respectively.

He possesses over a dozen years of industrial experience with Nortel Networks Wireless Infrastructure Group (now part of Ericsson), Freescale, and NXP Semiconductors, Chandler, AZ, USA, where he was involved in advanced power amplifier design, transmitter architectures, and large signal device modeling in support of cellular and wireless communication technology. He is currently managing the Advanced RF Design Team, RF Business Unit, NXP Semiconductors. He holds 16 patents, awarded and pending.

Joseph Staudinger (F'11) is currently a Fellow with NXP Semiconductors, Chandler, AZ, USA. His current research interests include research and product development of RF power amplifiers, transmitters, receivers, and transmitter/PA linearization for cellular and wireless networks. He is also a Faculty Associate with Arizona State University, Tempe, AZ, USA. He has authored or co-authored over 50 publications and holds 62 U.S. and foreign patents.

Jeffrey K. Jones (M'05–SM'16) is currently an NXP Fellow, and a Senior Director of Advanced Design Technology with the RF Power Business Unit, NXP Semiconductor, Chandler, AZ, USA. He has spent the majority of his 34-year career in RF and microwave engineering with NXP Semiconductor, Freescale Semiconductors, and Motorola Inc. He has authored over 15 industry papers and holds 24 U.S. patents, and has an additional 15 pending. His current research interests include high-efficiency RF amplifiers, RF integration, and multiband cellular amplifiers.

Fadhel M. Ghannouchi (S'84–M'88–SM'93–F'07) is currently a Professor, an Alberta Innovates/Canada Research Chair, and the Founding Director of the iRadio Laboratory, Department of Electrical and Computer Engineering, University of Calgary, Calgary, AB, Canada. He held several invited positions with several academic and research institutions in Europe, North America, and Japan. He has provided consulting services to many microwave and wireless communications companies. He has authored or co-authored over 650 publications and holds 16 U.S. patents with 4 pending. His current research interests include microwave instrumentation and measurements, nonlinear modeling of microwave devices and communications systems, design of power- and spectrum-efficient microwave amplification systems, and design of intelligent RF transceivers for wireless and satellite communications.